The Astrophysical Journal, 866:159 (12pp), 2018 October 20 https://doi.org/10.3847/1538-4357/aadf35

Dust Emission in an Accretion-rate-limited Sample of $z \gtrsim 6$ Quasars

Bram P. Venemans[1], Roberto Decarli[1,2], Fabian Walter[1,3,4], Eduardo Bañados[5], Frank Bertoldi[6], Xiaohui Fan[7], Emanuele Paolo Farina[8], Chiara Mazzucchelli[1], Dominik Riechers[9], Hans-Walter Rix[1], Ran Wang[10], and Yujin Yang[11]
[1] Max-Planck Institute for Astronomy, Königstuhl 17, D-69117 Heidelberg, Germany; venemans@mpia.de
[2] Osservatorio di Astrofisica e Scienza dello Spazio di Bologna, via Gobetti 93/3, I-40129 Bologna, Italy
[3] Astronomy Department, California Institute of Technology, MC105-24, Pasadena, CA 91125, USA
[4] National Radio Astronomy Observatory, Pete V. Domenici Array Science Center, P.O. Box 0, Socorro, NM 87801, USA
[5] The Observatories of the Carnegie Institution for Science, 813 Santa Barbara Street, Pasadena, CA 91101, USA
[6] Argelander Institute for Astronomy, University of Bonn, Auf dem Hügel 71, D-53121 Bonn, Germany
[7] Steward Observatory, The University of Arizona, 933 North Cherry Avenue, Tucson, AZ 85721-0065, USA
[8] Department of Physics, Broida Hall, University of California, Santa Barbara, CA 93106-9530, USA
[9] Cornell University, 220 Space Sciences Building, Ithaca, NY 14853, USA
[10] Kavli Institute of Astronomy and Astrophysics at Peking University, 5 Yiheyuan Road, Haidian District, Beijing 100871, People's Republic of China
[11] Korea Astronomy and Space Science Institute, Daedeokdae-ro 776, Yuseong-gu Daejeon 34055, Republic of Korea
Received 2018 June 15; revised 2018 August 27; accepted 2018 September 2; published 2018 October 24

Abstract

We present Atacama Large Millimeter Array 1 mm observations of the rest-frame far-infrared (FIR) dust continuum in 27 quasars at redshifts $6.0 \lesssim z < 6.7$. We detect FIR emission at $\gtrsim 3\sigma$ in all quasar host galaxies with flux densities at ~1900 GHz in the rest-frame of $0.12 < S_{\rm rest,1900\,GHz} < 5.9$ mJy, with a median (mean) flux density of 0.88 mJy (1.59 mJy). The implied FIR luminosities range from $L_{\rm FIR} = (0.27\text{–}13) \times 10^{12}\,L_\odot$, with 74% of our quasar hosts having $L_{\rm FIR} > 10^{12}\,L_\odot$. The estimated dust masses are $M_{\rm dust} = 10^{7}\text{–}10^{9}\,M_\odot$. If the dust is heated only by star formation, then the star formation rates in the quasar host galaxies are between 50 and 2700 $M_\odot$ yr^{-1}. In the framework of the host galaxy–black hole coevolution model a correlation between ongoing black hole growth and star formation in the quasar host galaxy would be expected. However, combined with results from the literature to create a luminosity-limited quasar sample, we do not find a strong correlation between quasar UV luminosity (a proxy for ongoing black hole growth) and FIR luminosity (star formation in the host galaxy). The absence of such a correlation in our data does not necessarily rule out the coevolution model, and could be due to a variety of effects (including different timescales for black hole accretion and FIR emission).

Key words: galaxies: high-redshift – galaxies: star formation – galaxies: statistics – quasars: general

1. Introduction

Luminous quasars are powered by accretion onto supermassive black holes with mass $\gtrsim 10^{8\text{–}9}\,M_\odot$. Such luminous quasars have been found out to very high redshift (the current quasar record holder is at $z = 7.54$ at a cosmic age of 690 Myr after the Big Bang; Bañados et al. 2018). In the local universe relations have been found between the mass of the central black hole and both the mass of the bulge (e.g., Kormendy & Ho 2013) and the mass of the galaxy (e.g., Reines & Volonteri 2015). If such relations were already in place at high redshift, the host galaxies of the distant quasars would be among the most massive galaxies at these early epochs.

Due to the bright central source, detecting the host galaxy of luminous distant quasars in the rest-frame UV or optical has proven to be very challenging (e.g., Decarli et al. 2012; Mechtley et al. 2012). On the other hand, already more than a decade ago studies at rest-frame far-infrared (FIR) wavelengths (redshifted to the observed (sub-)mm) have revealed intense FIR emission coming from the quasar host galaxies (e.g., Priddey & McMahon 2001; Bertoldi et al. 2003a; Walter et al. 2003; Maiolino et al. 2005; Beelen et al. 2006). Studying the quasar host galaxies in the (sub-)mm would therefore allow one to characterize the build-up and formation models of massive galaxies. Early bolometer work showed that ~30% of the $z \gtrsim 6$ quasars from the Sloan Digital Sky Survey (SDSS) were individually detected with flux densities of $S_{\rm obs,250\,GHz} \gtrsim 1.2$ mJy (Wang et al. 2008), indicating ultraluminous infrared galaxy (ULIRG)-like FIR luminosities of $L_{\rm FIR} > 10^{12\text{–}13}\,L_\odot$. Consequently, early efforts to characterize the host galaxies of $z \sim 6$ quasars concentrated on these FIR luminous quasars (e.g., Bertoldi et al. 2003b; Walter et al. 2003, 2004, 2009; Riechers et al. 2009; Wang et al. 2010, 2011a, 2013).

Later, Omont et al. (2013) and Willott et al. (2013, 2015) followed up a sample of quasars from the Canada-France-Hawaii Quasar Survey (CFHQS) with lower luminosities (~2 mag fainter) than the SDSS quasar. They found that the lower-luminosity quasars are, on average, fainter than the SDSS quasars with $S_{\rm obs,250\,GHz} < 1$ mJy. At the same time, our group started a pilot project targeting all quasars at $z > 6.5$ in the (sub-)mm. Initial results showed that luminous quasars can have a range of properties (Venemans et al. 2012, 2017a; Bañados et al. 2015) compared to the well-studied SDSS quasars. In Venemans et al. (2016) we reported a tentative correlation between FIR luminosity (a proxy for star formation) and the bolometric luminosity (a proxy for black hole growths) of the quasars.

To obtain a less biased view of the host galaxies of $z > 6$ quasars and to investigate how the quasar bolometric and FIR luminosities relate to each other, we targeted a UV luminosity-limited quasar sample with the Atacama Large Millimeter Array (ALMA). The properties of the [C II] 158 μm emission lines detected from the quasars in our sample are published in Decarli et al. (2018). From the quasar sample, 85% were detected in [C II] at a significance of $>5\sigma$, with typical luminosities of $L_{\rm [C\,II]} = 10^{9\text{–}10}\,L_\odot$ (Decarli et al. 2018). In

Table 1
Properties of the Quasars Targeted in the ALMA Survey

Name	R.A. (J2000)	Decl. (J2000)	Redshift	Method[a]	M_{1450}	References[b]
P007+04	$00^h28^m06\overset{s}{.}560$	+04°57′25.″39	6.0008 ± 0.0004	[C II]	−26.58	1, 2
P009–10	$00^h38^m56\overset{s}{.}527$	−10°25′54.″08	6.0039 ± 0.0004	[C II]	−26.50	1, 2
J0046–2837	$00^h46^m23\overset{s}{.}662$	−28°37′47.″44	5.99 ± 0.05	Template	−25.42	3, 3
J0142–3327	$01^h42^m43\overset{s}{.}710$	−33°27′45.″55	6.3379 ± 0.0004	[C II]	−27.76	1, 2
P065–26	$04^h21^m38\overset{s}{.}048$	−26°57′15.″60	6.1877 ± 0.0005	[C II]	−27.21	1, 2
P065–19	$04^h22^m00\overset{s}{.}999$	−19°27′28.″63	6.1247 ± 0.0006	[C II]	−26.57	1, 2
J0454–4448	$04^h54^m01\overset{s}{.}789$	−44°48′31.″26	6.0581 ± 0.0006	[C II]	−26.41	1, 2
J0842+1218	$08^h42^m29\overset{s}{.}429$	+12°18′50.″43	6.0763 ± 0.0005	[C II]	−26.85	1, 2
J1030+0524	$10^h30^m27\overset{s}{.}098$	+05°24′55.″00	6.308 ± 0.001	Mg II	−26.93	4, 2
P159–02	$10^h36^m54\overset{s}{.}193$	−02°32′37.″85	6.3809 ± 0.0005	[C II]	−26.74	1, 2
J1048–0109	$10^h48^m19\overset{s}{.}081$	−01°09′40.″45	6.6759 ± 0.0005	[C II]	−25.96	1, 5
P167–13	$11^h10^m33\overset{s}{.}988$	−13°29′45.″84	6.5148 ± 0.0005	[C II]	−25.57	1, 6
J1148+0702	$11^h48^m03\overset{s}{.}286$	+07°02′08.″33	6.339 ± 0.001	Mg II	−26.43	7, 2
J1152+0055	$11^h52^m21\overset{s}{.}277$	+00°55′36.″54	6.3643 ± 0.0005	[C II]	−25.08[c]	1, 2
J1207+0630	$12^h07^m37\overset{s}{.}428$	+06°30′10.″17	6.0366 ± 0.0009	[C II]	−26.57	1, 2
P183+05	$12^h12^m26\overset{s}{.}974$	+05°05′33.″59	6.4386 ± 0.0004	[C II]	−26.99	1, 6
J1306+0356	$13^h06^m08\overset{s}{.}284$	+03°56′26.″25	6.0337 ± 0.0004	[C II]	−26.76	1, 2
P217–16	$14^h28^m21\overset{s}{.}371$	−16°02′43.″73	6.1498 ± 0.0011	[C II]	−26.89	1, 2
J1509–1749	$15^h09^m41\overset{s}{.}781$	−17°49′26.″68	6.1225 ± 0.0007	[C II]	−27.09	1, 2
P231–20	$15^h26^m37\overset{s}{.}841$	−20°50′00.″66	6.5864 ± 0.0005	[C II]	−27.14	1, 6
P308–21	$20^h32^m10\overset{s}{.}003$	−21°14′02.″25	6.2341 ± 0.0005	[C II]	−26.30	1, 2
J2100–1715	$21^h00^m54\overset{s}{.}707$	−17°15′21.″88	6.0812 ± 0.0005	[C II]	−25.50	1, 2
J2211–3206	$22^h11^m12\overset{s}{.}417$	−32°06′12.″54	6.3394 ± 0.0010	[C II]	−26.65	1, 3
P340–18	$22^h40^m48\overset{s}{.}978$	−18°39′43.″62	6.01 ± 0.05	Template	−26.36	2, 2
J2318–3113	$23^h18^m18\overset{s}{.}393$	−31°13′46.″56	6.4435 ± 0.0005	[C II]	−26.06	1, 3
J2318–3029	$23^h18^m33\overset{s}{.}099$	−30°29′33.″51	6.1458 ± 0.0004	[C II]	−26.16	1, 3
P359–06	$23^h56^m32\overset{s}{.}439$	−06°22′59.″18	6.1722 ± 0.0004	[C II]	−26.74	1, 2

Notes.
[a] Method used to determine the redshift, with "Template" referring to a template fit to the rest-frame UV quasar spectrum.
[b] References for the redshift and M_{1450}: (1) Decarli et al. (2018), (2) Bañados et al. (2016), (3) B. P. Venemans et al. (2018, in preparation), (4) Kurk et al. (2007), (5) Wang et al. (2017), (6) Mazzucchelli et al. (2017), (7) Jiang et al. (2016).
[c] After creating the sample, additional analysis of the optical spectrum of this quasar decreased the absolute magnitude below our luminosity cut (Section 2.1).

Decarli et al. (2017) we reported the discovery of [C II]-emitting companion sources near some of our quasars. In this paper, we will focus on the dust continuum emission of our sample of high-redshift quasars. The paper is organized as follows. In Section 2.1 we will introduce the sample followed by a brief description of the ALMA observations in Section 2.2 and the literature sample in Section 2.3. Our results are described in Section 3 and the derived characteristics are discussed in Section 4. Finally, we summarize our findings in Section 5.

Throughout this paper all magnitudes are on the AB system. We adopt a concordance cosmology with $\Omega_M = 0.3$, $\Omega_\Lambda = 0.7$, and $H_0 = 70\,\mathrm{km\,s^{-1}\,Mpc^{-1}}$, which is consistent with measurements from *Planck* (Planck Collaboration et al. 2016). Star formation rates (SFRs) are calculated assuming a Kroupa & Weidner (2003) initial mass function.

2. The Sample and New Observations

2.1. A Quasar Luminosity-limited Sample

To study the range of FIR properties displayed in the host galaxies of $z \sim 6$ quasars, we created a luminosity-limited sample. Based on the luminosity limit of quasars found in wide area sky surveys (e.g., Bañados et al. 2016; Jiang et al. 2016), we selected quasars with an absolute UV magnitude brighter than $M_{1450} < -25.25$, approximately corresponding to a black hole mass $M_{\rm BH} > 2.5 \times 10^8\,M_\odot$ (assuming Eddington accretion). We further set a lower redshift cut of $z > 5.94$ to ensure that the [C II] 158 μm emission line is redshifted to the easily accessible 1.2 mm band (ALMA band 6). Finally, to allow observations at low airmass with ALMA, we set a declination limit of $<+15°$. In 2015 April (when we created the sample), the sample consisted of 43 quasars, of which 9 were unpublished at the time.

Of the 43 quasars in our luminosity-limited sample, 8 were already observed in [C II] with sensitive interferometers, such as ALMA and IRAM/PdBI. The final target list for our ALMA quasar survey thus consisted of 35 sources.[12] Of these, 27 were observed with ALMA in Cycle 3 (see Decarli et al. 2018, for more details). The remaining 8 sources were not observed, mostly due to poor visibility when ALMA was in a suitable array configuration. The coordinates, redshifts, and optical properties of the 27 observed quasars are listed in Table 1 and a brief description of the observations is given in the next section.

2.2. ALMA Observations and Analysis

The new ALMA observations (program ID: 2015.1.01115.S, PI: F. Walter) consisted of 8 min on-source integrations with two (partly overlapping) bandpasses of 1.875 GHz covering the redshifted [C II] 158 μm line and two bandpasses of 1.875 GHz width each targeting the quasar continuum at slightly lower

[12] Additional analysis of one of the quasars in our sample, J1152+0055, by Bañados et al. (2016) resulted in an absolute magnitude 0.17 mag below our limit of $M_{1450} = -25.25$ (Table 1). We decided to keep it in our sample.

frequencies. The typical beam had a size of $\sim 1\farcs0$ and the typical rms noise is 0.5 mJy beam^{-1} in 30 km s^{-1} bins. Further details of the observations and the data reduction can be found in Decarli et al. (2018).

We generated two continuum maps for each source. One was created by averaging the line-free channels in the two spectral windows targeting the [C II] line (see Decarli et al. 2018, for details). This map provides measurements of the continuum flux density of the quasar host at a rest-frame frequency of 1900 GHz, $S_{\rm rest,1900\,GHz}$. The second map was constructed by averaging all the channels in the spectral windows in the lower sideband, covering a frequency typically $\sim$16 GHz lower than that of the [C II] line. The flux densities measured in this map will be referred to as $S_{\rm rest,1790\,GHz}$. For objects that were not detected in these maps, we created a continuum map by averaging all line-free channels of the four bandpasses (see below).

To determine the continuum flux densities of the quasar host galaxies, we performed the following steps. First, the peak flux density in the maps was measured by selecting the brightest pixel within $0\farcs5$ of the quasar position (Table 1). We also measured the source brightness and extent using the CASA task "imfit." If the S/N ratio of the peak flux density in one of the continuum maps was at least 7, then the integrated flux densities provided by "imfit" were taken as the brightness of the source as listed in Table 2. In the other cases a brightness equal to the peak flux density was adopted as the fits provided by "imfit" became poorly constrained. In four cases, for J0046–2837, J1030+0524, J1152+0055, and P340–18, the S/N of the peak pixel was below 3 in our deeper continuum map (the one covering the frequencies around 1790 GHz in the rest-frame). In these cases, we created an additional continuum map by averaging all line-free channels in all four spectral windows and determined the peak flux density within $0\farcs5$ of the quasar position. In these new maps, the four faint quasar hosts were potentially detected at a significance of $\sim 3\sigma$–4σ (Table 2). In Figure 1 we show postage stamps for our sample.

2.3. Literature Sample

From the literature we collected all available observations of high-redshift ($z > 5.7$) quasars obtained in the 1 mm band. These observations include both bolometer observations (with the IRAM 30 m/MAMBO, Bertoldi et al. 2003a; Petric et al. 2003; Wang et al. 2007, 2008, 2011b; Omont et al. 2013) and interferometric observations with ALMA (Wang et al. 2013, 2016; Willott et al. 2013, 2015, 2017; Venemans et al. 2016, 2017a) and the PdBI/NOEMA (Gallerani et al. 2014; Bañados et al. 2015; Mazzucchelli et al. 2017; Venemans et al. 2017b). In total, 64 quasars with mm observations were found in the literature, of which 30 were detected. Most of the non-detections came from the bolometer observations, which typically had 1σ noise levels of 0.5–1.0 mJy. A summary of the optical and FIR properties of the quasars with literature measurements is listed in Table 3.

3. Results

We detect all 27 quasar hosts in the dust continuum (Figure 1) at a significance of $\gtrsim 3\sigma$, of which 21 (78%) have a peak flux density with an S/N > 5. The flux densities span a range of a factor $\sim$50, from 0.12 to $\sim$6 mJy. In several fields, additional sources adjacent to the quasars are visible. These objects are discussed in separate papers (Decarli et al. 2017; Champagne et al. 2018). In Table 2 we list the continuum brightness of all the quasars and the measured sizes for the objects detected at S/N > 7. In the next section (Section 3.1) we will discuss the extent of the continuum emission. In Section 3.2 we will compare the properties of the quasars in our sample with those from the literature.

3.1. Continuum Emission Size

In Figure 2 we show the ratio of the beam-convolved major axis of the continuum emission of the quasars and the beam size a function of the S/N of the continuum emission. Following Decarli et al. (2018), we only regard objects detected at S/N > 10 as suitable to determine the extent of the emission. Of the quasars in our sample, 16 are detected with a S/N > 10 at a rest-frame frequency of 1790 GHz. At the resolution of our observations (typically $1\farcs1 \times 0\farcs9$, or 6.2×5.1 kpc^2), none of the sources are resolved with measured sizes >2× the beam. Of the 16 high S/N sources, 10 (62.5%) have an observed major axis less than 1.2 times the major axis of the beam. We consider these objects unresolved, as the measured size is within 1σ–2σ of the size of the beam. Six quasars (37.5%) are marginally resolved, with measured major axis size between 1.2 and 1.6 times that of the beam. The deconvolved sizes are in the range 3.3–6.9 kpc, with significant uncertainties. To more accurately estimate the range of sizes of the quasar host galaxies, higher-resolution imaging is required (e.g., Shao et al. 2017; Venemans et al. 2017a). Despite the large uncertainties, the sizes of the quasar host galaxies appear to be similar to those of star-forming galaxies at $z = 2$ (e.g., Tadaki et al. 2017). Furthermore, we note that only a fraction ($\sim$15%) of the sources studied here show signatures of a recent merger and/or a very nearby companion galaxy (see Decarli et al. 2017). This relatively small fraction seems to be at odds with the model that the AGN activity and the (obscured) star formation are triggered by a merger (e.g., Sanders et al. 1988; Hopkins et al. 2008; Alexander & Hickox 2012), although imaging with a higher spatial resolution is needed to exclude very close companions and/or very compact merger remnants.

3.2. Sample Properties

In Figure 3 we show the histograms of observed continuum flux densities of the quasar host galaxies in our sample and from the literature. When compared to quasars previously observed at 1 mm, our survey covers nearly the full range of flux densities. The mean flux density of our sample is $\langle S_{\rm obs,1\,mm}\rangle = 1.6$ mJy, very similar to the mean flux density of luminous $z \sim 6$ quasars of 1.26 mJy reported by Wang et al. (2008) based on MAMBO bolometer observations. The mean flux density of our sample is dominated by a handful of bright quasars with $S_{\rm obs,1\,mm} > 1$ mJy. The median flux density of our sample is 0.88 mJy, which is only slightly higher than the average flux density of $z \sim 6$ quasar hosts that were not individually detected by MAMBO ($S_{\rm obs,250\,GHz} = 0.52 \pm 0.13$ mJy, Wang et al. 2008). This is not too surprising, as the Wang et al. (2008) sample of quasars overlaps with ours (see Section 2.1).

A sample of, on average, less luminous (in the rest-frame UV) quasars from the CFHQS at $5.8 < z < 6.5$ was observed by Omont et al. (2013) using the MAMBO bolometer. Only a single source was detected at an S/N > 3 and the stacked 1 mm flux density of the sample was $\langle S_{\rm obs,1\,mm}({\rm CFHQS})\rangle = 0.41$ mJy (after removing the single detection). Although the average

Table 2
Measured and Derived Properties of the Quasars in Our Sample

Name	S/N (at 1790 GHz)	S/N (at 1900 GHz)	$S_{\rm rest,1790\ GHz}$ (mJy)	$S_{\rm rest,1900\ GHz}$ (mJy)	Size (at 1790 GHz)	Size (at 1900 GHz)	log $L_{\rm FIR}$[a] ($L_\odot$)	SFR[a,b] ($M_\odot$ yr^{-1})	log $M_{\rm dust}$[a] ($M_\odot$)
P007+04	28	26	3.280 ± 0.220	3.880 ± 0.260	0.″58 × 0.″28	0.″54 × 0.″23	12.87	1564	8.68
P009–10	22	20	4.310 ± 0.300	4.510 ± 0.360	0.″86 × 0.″53	0.″72 × 0.″46	12.94	1808	8.74
J0046–2837	1	2	0.128 ± 0.039[c]	(3.3σ)	⋯	⋯	11.43	56	7.23
J0142–3327	21	19	1.810 ± 0.140	2.540 ± 0.180	0.″92 × 0.″36	0.″78 × 0.″57	12.73	1130	8.54
P065–26	13	14	1.040 ± 0.130	1.650 ± 0.140	0.″73 × 0.″25	0.″69 × 0.″37	12.53	702	8.33
P065–19	7	8	0.561 ± 0.124	0.482 ± 0.094	0.″97 × 0.″84	<1.″08 × 0.″71	11.98	202	7.79
J0454–4448	12	12	0.672 ± 0.080	0.992 ± 0.137	0.″62 × 0.″22	0.″62 × 0.″48	12.30	417	8.10
J0842+1218	10	6	0.542 ± 0.064	0.732 ± 0.223	0.″65 × 0.″10	1.″29 × 0.″15	12.16	304	7.97
J1030+0524	2	2	0.134 ± 0.046[c]	(2.9σ)	⋯	⋯	11.49	64	7.29
P159–02	11	11	0.646 ± 0.086	0.679 ± 0.091	0.″73 × 0.″44	<1.″23 × 0.″94	12.16	305	7.97
J1048–0109	41	38	2.722 ± 0.094	3.110 ± 0.120	0.″61 × 0.″33	0.″53 × 0.″30	12.85	1500	8.66
P167–13	11	14	0.749 ± 0.091	1.071 ± 0.092	1.″02 × 0.″71	0.″95 × 0.″46	12.38	502	8.18
J1148+0702	4	7	0.494 ± 0.168	0.664 ± 0.181	1.″89 × 0.″80	1.″37 × 0.″30	12.15	293	7.95
J1152+0055	2	4	0.124 ± 0.043[c]	(2.9σ)	⋯	⋯	11.45	60	7.26
J1207+0630	6	5	0.407 ± 0.064	0.467 ± 0.091	⋯	⋯	11.96	192	7.77
P183+05	42	41	4.770 ± 0.140	5.850 ± 0.160	0.″58 × 0.″48	0.″62 × 0.″40	13.11	2693	8.91
J1306+0356	15	12	1.250 ± 0.100	1.480 ± 0.220	1.″20 × 0.″37	1.″05 × 0.″45	12.46	605	8.26
P217–16	5	4	0.350 ± 0.070	0.421 ± 0.100	⋯	⋯	11.93	178	7.73
J1509–1749	23	20	1.365 ± 0.089	1.760 ± 0.110	<1.″44 × 0.″93	<1.″35 × 0.″87	12.55	742	8.35
P231–20	36	84	3.920 ± 0.450	4.210 ± 0.360	0.″61 × 0.″52	0.″31 × 0.″25	12.99	2026	8.79
P308–21	17	6	0.846 ± 0.080	0.824 ± 0.203	0.″83 × 0.″58	1.″67 × 0.″73	12.23	358	8.04
J2100–1715	7	5	0.554 ± 0.140	0.877 ± 0.248	<0.″78 × 0.″66	0.″83 × 0.″33	12.24	366	8.05
J2211–3206	11	9	0.689 ± 0.075	0.733 ± 0.121	0.″58 × 0.″29	<0.″87 × 0.″69	12.19	326	8.00
P340–18	3	4	0.174 ± 0.046[c]	(3.8σ)	⋯	⋯	11.56	76	7.36
J2318–3113	5	5	0.418 ± 0.087	0.567 ± 0.105	⋯	⋯	12.10	261	7.90
J2318–3029	26	24	3.190 ± 0.200	3.930 ± 0.220	0.″71 × 0.″38	0.″79 × 0.″35	12.90	1653	8.70
P359–06	8	7	0.982 ± 0.170	1.020 ± 0.210	<1.″14 × 0.″64	0.″79 × 0.″22	12.32	436	8.12

Notes.
[a] Quoted uncertainties are measurement errors, assuming the dust spectral energy distribution can be described by a modified blackbody with $T_{\rm dust} = 47$ K, $\beta = 1.6$, and a negligible dust optical depth at $\nu_{\rm rest} = 1790$ GHz. The actual uncertainties are dominated by our assumptions on the shape of the dust spectral energy distribution (see Sections 4.1–4.3 for a detailed discussion).
[b] Assuming the dust is heated only by star formation (see Section 4.2).
[c] These flux densities were measured in a map created by averaging all four spectral windows.

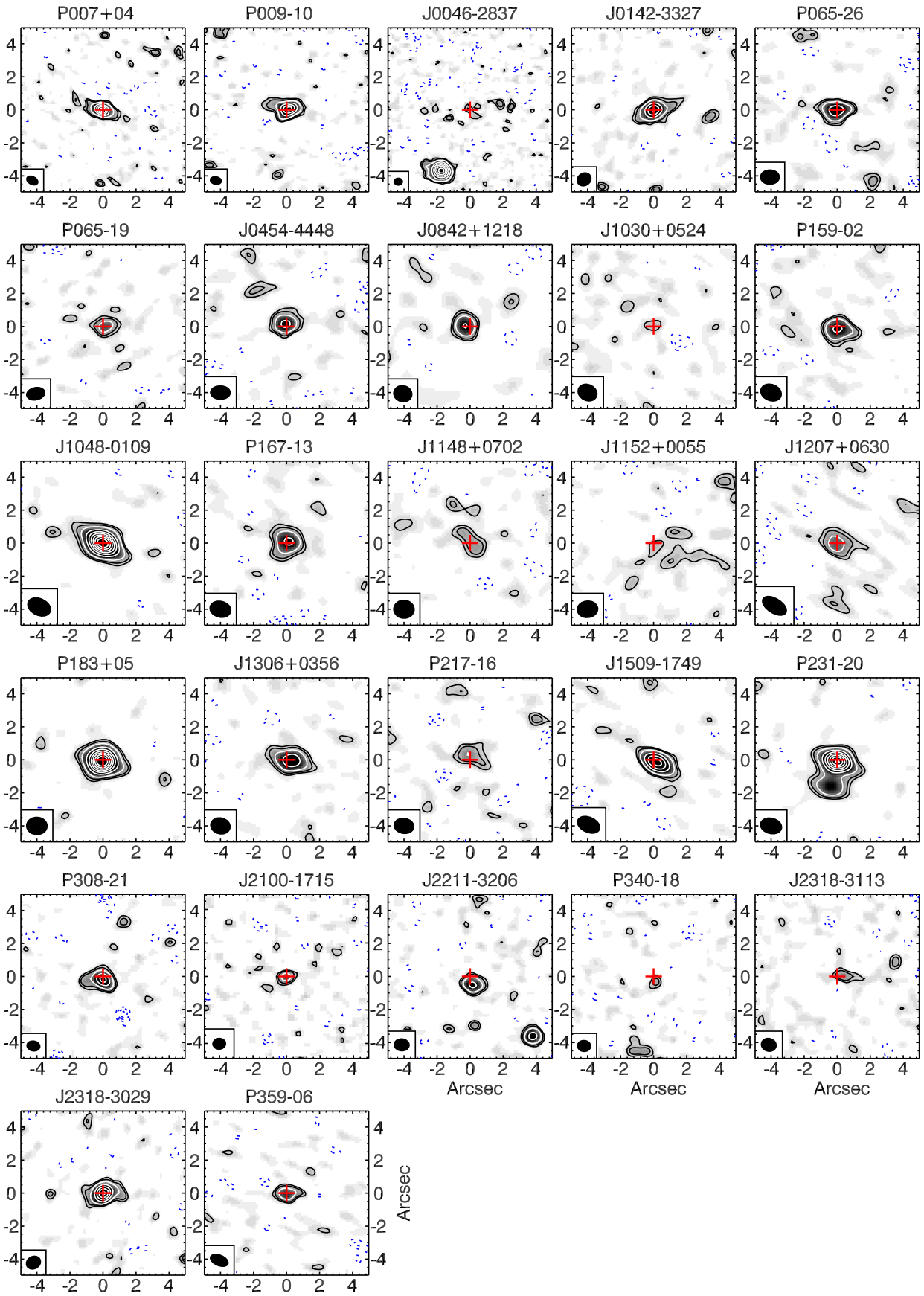

Figure 1. Continuum maps of the 27 quasars observed in our survey. The postage stamps are $10'' \times 10''$ in size. The maps were created by averaging the channels in the spectral windows in the lower sideband, away from the [C II] line, probing a rest-frame frequency around 1790 GHz. The optical positions of the quasars are indicated with a red cross. The dashed contours are -3σ and -2σ and the solid contours are $+2\sigma$, $+3\sigma$ and [5, 10, 15, 20, 25, 30, 35] $\times\ \sigma$.

Table 3
Quasars in the Literature with Observations at 1 mm

Name	R.A. (J2000)	Decl. (J2000)	Redshift	M_{1450}	$S_{\rm obs,1\ mm}$ (mJy)	References[a]
J0002+2550	$00^{\rm h}02^{\rm m}39\overset{\rm s}{.}39$	$+25°50'34\overset{''}{.}8$	5.82	−27.26	<2.64	1, 2, 3
J0005–0006	$00^{\rm h}05^{\rm m}52\overset{\rm s}{.}34$	$-00°06'55\overset{''}{.}8$	5.844	−25.67	<1.44	4, 2, 5
P006+39	$00^{\rm h}24^{\rm m}29\overset{\rm s}{.}772$	$+39°13'18\overset{''}{.}98$	6.6210	−26.85	0.55 ± 0.18	6, 6, 6
J0033–0125	$00^{\rm h}33^{\rm m}11\overset{\rm s}{.}40$	$-01°25'24\overset{''}{.}9$	6.13	−25.09	1.13 ± 0.36	7, 2, 5
J0050+3445	$00^{\rm h}50^{\rm m}06\overset{\rm s}{.}67$	$+34°45'22\overset{''}{.}6$	6.253	−26.65	<2.28	8, 2, 9
J0055+0146	$00^{\rm h}55^{\rm m}02\overset{\rm s}{.}92$	$+01°46'17\overset{''}{.}8$	6.0060	−24.76	0.21 ± 0.03	10, 2, 10
J0100+2802	$01^{\rm h}00^{\rm m}13\overset{\rm s}{.}02$	$+28°02'25\overset{''}{.}8$	6.3258	−29.09	1.35 ± 0.25	11, 2, 11
J0102–0218	$01^{\rm h}02^{\rm m}50\overset{\rm s}{.}64$	$-02°18'09\overset{''}{.}9$	5.95	−24.54	<1.14	12, 2, 9
J0109–3047	$01^{\rm h}09^{\rm m}53\overset{\rm s}{.}13$	$-30°47'26\overset{''}{.}32$	6.7909	−25.59	0.56 ± 0.11	13, 2, 13
J0129–0035	$01^{\rm h}29^{\rm m}58\overset{\rm s}{.}51$	$-00°35'39\overset{''}{.}7$	5.7787	−23.83	2.57 ± 0.06	14, 2, 14
J0136+0226	$01^{\rm h}36^{\rm m}03\overset{\rm s}{.}17$	$+02°26'05\overset{''}{.}7$	6.21	−24.60	<2.91	15, 2, 9
J0203+0012	$02^{\rm h}03^{\rm m}32\overset{\rm s}{.}39$	$+00°12'29\overset{''}{.}3$	5.72	−26.20	1.85 ± 0.46	16, 2, 17
J0210–0456	$02^{\rm h}10^{\rm m}13\overset{\rm s}{.}19$	$-04°56'20\overset{''}{.}9$	6.4323	−24.47	0.12 ± 0.04	18, 2, 18
J0216–0455	$02^{\rm h}16^{\rm m}27\overset{\rm s}{.}81$	$-04°55'34\overset{''}{.}1$	6.01	−22.43	<0.04	12, 2, 19
J0221–0802	$02^{\rm h}21^{\rm m}22\overset{\rm s}{.}718$	$-08°02'51\overset{''}{.}62$	6.161	−24.65	0.25 ± 0.05	8, 2, 19
P036+03	$02^{\rm h}26^{\rm m}01\overset{\rm s}{.}876$	$+03°02'59\overset{''}{.}39$	6.5412	−27.28	2.50 ± 0.50	20, 6, 20
J0227–0605	$02^{\rm h}27^{\rm m}43\overset{\rm s}{.}29$	$-06°05'30\overset{''}{.}2$	6.20	−25.23	<1.59	12, 2, 9
J0239–0045	$02^{\rm h}39^{\rm m}30\overset{\rm s}{.}24$	$-00°45'05\overset{''}{.}4$	5.82	−24.49	<1.62	21, 2, 17
J0303–0019	$03^{\rm h}03^{\rm m}31\overset{\rm s}{.}40$	$-00°19'12\overset{''}{.}9$	6.078	−25.50	<1.53	22, 2, 5
J0305–3150	$03^{\rm h}05^{\rm m}16\overset{\rm s}{.}91$	$-31°50'55\overset{''}{.}94$	6.6145	−26.13	3.29 ± 0.10	13, 2, 13
J0316–1340	$03^{\rm h}16^{\rm m}49\overset{\rm s}{.}87$	$-13°40'32\overset{''}{.}2$	5.99	−24.85	<4.32	15, 2, 9
J0353+0104	$03^{\rm h}53^{\rm m}49\overset{\rm s}{.}76$	$+01°04'05\overset{''}{.}4$	6.072	−26.37	<1.38	4, 2, 5
J0818+1722	$08^{\rm h}18^{\rm m}27\overset{\rm s}{.}40$	$+17°22'51\overset{''}{.}8$	6.02	−27.46	1.19 ± 0.38	1, 2, 5
J0836+0054	$08^{\rm h}36^{\rm m}43\overset{\rm s}{.}85$	$+00°54'53\overset{''}{.}3$	5.810	−27.69	<2.88	23, 2, 24
J0840+5624	$08^{\rm h}40^{\rm m}35\overset{\rm s}{.}09$	$+56°24'19\overset{''}{.}9$	5.85	−27.19	3.20 ± 0.64	25, 2, 3
J0841+2905	$08^{\rm h}41^{\rm m}19\overset{\rm s}{.}52$	$+29°05'04\overset{''}{.}5$	5.98	−26.45	<1.29	1, 2, 5
J0859+0022	$08^{\rm h}59^{\rm m}07\overset{\rm s}{.}19$	$+00°22'55\overset{''}{.}9$	6.3903	−24.09	0.16 ± 0.02	26, 27, 26
J0927+2001	$09^{\rm h}27^{\rm m}21\overset{\rm s}{.}82$	$+20°01'23\overset{''}{.}7$	5.79	−26.71	4.98 ± 0.75	25, 2, 3
J1044–0125	$10^{\rm h}44^{\rm m}33\overset{\rm s}{.}04$	$-01°25'02\overset{''}{.}2$	5.7847	−27.33	3.12 ± 0.09	14, 2, 14
J1048+4637	$10^{\rm h}48^{\rm m}45\overset{\rm s}{.}05$	$+46°37'18\overset{''}{.}3$	6.198	−27.19	3.00 ± 0.40	4, 2, 28
J1059–0906	$10^{\rm h}59^{\rm m}28\overset{\rm s}{.}61$	$-09°06'20\overset{''}{.}4$	5.92	−25.81	<2.46	15, 2, 9
J1120+0641	$11^{\rm h}20^{\rm m}01\overset{\rm s}{.}465$	$+06°41'23\overset{''}{.}81$	7.0851	−26.58	0.53 ± 0.04	29, 2, 29
J1137+3549	$11^{\rm h}37^{\rm m}17\overset{\rm s}{.}73$	$+35°49'56\overset{''}{.}9$	6.03	−27.30	<3.39	1, 2, 3
J1148+5251	$11^{\rm h}48^{\rm m}16\overset{\rm s}{.}64$	$+52°51'50\overset{''}{.}2$	6.4190	−27.56	4.00 ± 0.10	30, 2, 31
J1202–0057	$12^{\rm h}02^{\rm m}46\overset{\rm s}{.}37$	$-00°57'01\overset{''}{.}7$	5.9289	−22.83	0.25 ± 0.01	26, 27, 26
J1205–0000	$12^{\rm h}05^{\rm m}05\overset{\rm s}{.}098$	$-00°00'27\overset{''}{.}97$	6.730	−24.90	0.83 ± 0.18	6, 6, 6
J1250+3130	$12^{\rm h}50^{\rm m}51\overset{\rm s}{.}93$	$+31°30'21\overset{''}{.}9$	6.15	−26.47	<2.70	1, 2, 3
J1319+0950	$13^{\rm h}19^{\rm m}11\overset{\rm s}{.}29$	$+09°50'51\overset{''}{.}4$	6.1330	−26.99	5.23 ± 0.10	14, 2, 14
J1335+3533	$13^{\rm h}35^{\rm m}50\overset{\rm s}{.}81$	$+35°33'15\overset{''}{.}8$	5.95	−26.63	2.34 ± 0.50	25, 2, 3
J1342+0928	$13^{\rm h}42^{\rm m}08\overset{\rm s}{.}097$	$+09°28'38\overset{''}{.}28$	7.5413	−26.80	0.41 ± 0.07	32, 33, 32
J1411+1217	$14^{\rm h}11^{\rm m}11\overset{\rm s}{.}29$	$+12°17'37\overset{''}{.}4$	5.904	−26.64	<1.86	23, 2, 3
J1425+3254	$14^{\rm h}25^{\rm m}16\overset{\rm s}{.}30$	$+32°54'09\overset{''}{.}0$	5.85	−26.40	2.27 ± 0.51	34, 2, 5
J1427+3312	$14^{\rm h}27^{\rm m}38\overset{\rm s}{.}59$	$+33°12'42\overset{''}{.}0$	6.12	−26.05	<1.98	35, 2, 5
J1429+5447	$14^{\rm h}29^{\rm m}52\overset{\rm s}{.}17$	$+54°47'17\overset{''}{.}6$	6.21	−26.05	3.46 ± 0.52	15, 2, 9
J1436+5007	$14^{\rm h}36^{\rm m}11\overset{\rm s}{.}74$	$+50°07'06\overset{''}{.}9$	5.85	−26.50	<3.42	1, 2, 3
J1602+4228	$16^{\rm h}02^{\rm m}53\overset{\rm s}{.}98$	$+42°28'24\overset{''}{.}9$	6.09	−26.89	<1.62	1, 2, 5
J1621+5155	$16^{\rm h}21^{\rm m}00\overset{\rm s}{.}70$	$+51°55'44\overset{''}{.}8$	5.71	−27.07	<1.65	36, 2, 5
J1623+3112	$16^{\rm h}23^{\rm m}31\overset{\rm s}{.}81$	$+31°12'00\overset{''}{.}5$	6.2605	−26.50	<2.40	37, 2, 3
J1630+4012	$16^{\rm h}30^{\rm m}33\overset{\rm s}{.}90$	$+40°12'09\overset{''}{.}6$	6.058	−26.14	<1.80	4, 2, 28
J1641+3755	$16^{\rm h}41^{\rm m}21\overset{\rm s}{.}64$	$+37°55'20\overset{''}{.}5$	6.047	−25.62	<1.41	8, 2, 9
J2053+0047	$20^{\rm h}53^{\rm m}21\overset{\rm s}{.}77$	$+00°47'06\overset{''}{.}8$	5.92	−25.23	<1.89	21, 2, 17
J2054–0005	$20^{\rm h}54^{\rm m}06\overset{\rm s}{.}42$	$-00°05'14\overset{''}{.}8$	6.0391	−26.54	2.98 ± 0.05	14, 2, 14
P323+12	$21^{\rm h}32^{\rm m}33\overset{\rm s}{.}191$	$+12°17'55\overset{''}{.}26$	6.5881	−27.06	0.47 ± 0.15	6, 6, 6
J2147+0107	$21^{\rm h}47^{\rm m}55\overset{\rm s}{.}40$	$+01°07'55\overset{''}{.}0$	5.81	−25.31	<1.83	21, 2, 17
J2216–0016	$22^{\rm h}16^{\rm m}44\overset{\rm s}{.}47$	$-00°16'50\overset{''}{.}1$	6.0962	−23.82	0.14 ± 0.03	26, 27, 26
VIMOS2911	$22^{\rm h}19^{\rm m}17\overset{\rm s}{.}227$	$+01°02'48\overset{''}{.}88$	6.1492	−22.54	0.77 ± 0.05	19, 2, 19
J2229+1457	$22^{\rm h}29^{\rm m}01\overset{\rm s}{.}66$	$+14°57'08\overset{''}{.}30$	6.1517	−24.72	<0.09	10, 2, 10
P338+29	$22^{\rm h}32^{\rm m}55\overset{\rm s}{.}150$	$+29°30'32\overset{''}{.}23$	6.6660	−26.08	0.97 ± 0.22	6, 6, 6
J2242+0334	$22^{\rm h}42^{\rm m}37\overset{\rm s}{.}55$	$+03°34'21\overset{''}{.}6$	5.88	−24.46	<1.83	15, 2, 9
J2307+0031	$23^{\rm h}07^{\rm m}35\overset{\rm s}{.}40$	$+00°31'49\overset{''}{.}0$	5.87	−25.22	<1.59	21, 2, 17
J2310+1855	$23^{\rm h}10^{\rm m}38\overset{\rm s}{.}88$	$+18°55'19\overset{''}{.}7$	6.0031	−27.75	8.91 ± 0.08	14, 2, 14
J2315–0023	$23^{\rm h}15^{\rm m}46\overset{\rm s}{.}36$	$-00°23'57\overset{''}{.}5$	6.12	−25.61	<1.80	38, 2, 5
J2318–0246	$23^{\rm h}18^{\rm m}02\overset{\rm s}{.}80$	$-02°46'34\overset{''}{.}0$	6.05	−25.05	<1.68	12, 2, 9
J2329–0301	$23^{\rm h}29^{\rm m}08\overset{\rm s}{.}28$	$-03°01'58\overset{''}{.}8$	6.4164	−25.19	<0.06	19, 2, 19

Table 3
(Continued)

Name	R.A. (J2000)	Decl. (J2000)	Redshift	M_{1450}	$S_{\rm obs,1\ mm}$ (mJy)	References[a]
J2329–0403	$23^{\rm h}29^{\rm m}14\overset{\rm s}{.}46$	$-04°03'24\overset{''}{.}1$	5.90	−24.60	<1.89	12, 2, 9
J2348–3054	$23^{\rm h}48^{\rm m}33\overset{\rm s}{.}35$	$-30°54'10\overset{''}{.}28$	6.9018	−25.75	1.92 ± 0.14	13, 2, 13
J2356+0023	$23^{\rm h}56^{\rm m}51\overset{\rm s}{.}58$	$+00°23'33\overset{''}{.}3$	6.00	−24.50	<1.47	21, 2, 17

Note.
[a] References for the redshift, M_{1450}, and $S_{\rm obs,1mm}$ data: (1) Carilli et al. (2010), (2) Bañados et al. (2016), (3) Wang et al. (2007), (4) De Rosa et al. (2011), (5) Wang et al. (2008), (6) Mazzucchelli et al. (2017), (7) Willott et al. (2007), (8) Willott et al. (2010a), (9) Omont et al. (2013), (10) Willott et al. (2015), (11) Wang et al. (2016), (12) Willott et al. (2009), (13) Venemans et al. (2016), (14) Wang et al. (2013), (15) Willott et al. (2010b), (16) Mortlock et al. (2009), (17) Wang et al. (2011b), (18) Willott et al. (2013), (19) Willott et al. (2017), (20) Bañados et al. (2015), (21) Jiang et al. (2009), (22) Kurk et al. (2009), (23) Kurk et al. (2007), (24) Petric et al. (2003), (25) Fan et al. (2006), (26) Izumi et al. (2018), (27) Matsuoka et al. (2018), (28) Bertoldi et al. (2003a), (29) Venemans et al. (2017a), (30) Walter et al. (2009), (31) Gallerani et al. (2014), (32) Venemans et al. (2017b), (33) Bañados et al. (2018), (34) Cool et al. (2006), (35) McGreer et al. (2006), (36) Jiang et al. (2016), (37) Wang et al. (2011a), (38) Jiang et al. (2008).

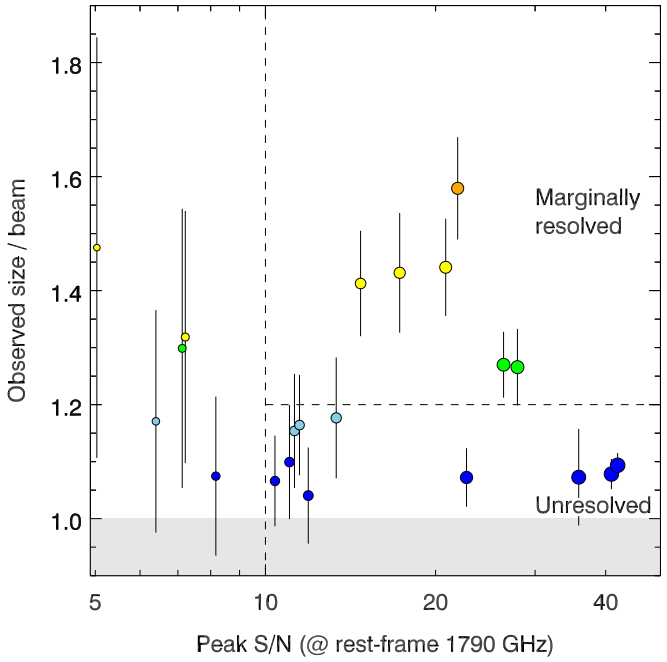

Figure 2. Observed continuum size (major axis from Table 2) divided by the beam size of the quasars in our sample as a function of peak S/N. The colors represent the ratio of observed size over the beam size. The size of the symbols scales with the S/N of the peak flux density. Sources with an observed size over the beam larger than ∼1.2 are considered marginally resolved.

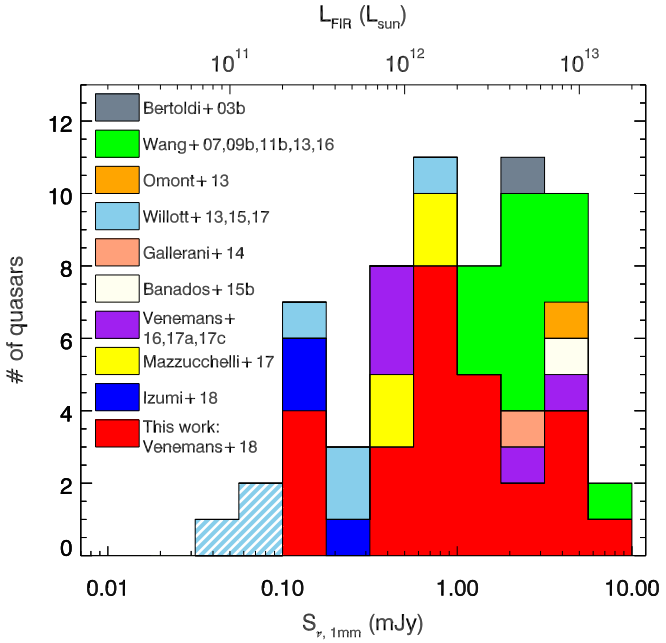

Figure 3. Distribution of the observed brightness of the $z \gtrsim 6$ quasar host galaxies in our sample (red histogram) at an observed wavelength (frequency) of ∼1 mm (∼250 GHz). For illustration, we show the corresponding FIR luminosity on the top axis for a source at the median redshift of our sample ($z = 6.1$) using a dust spectral energy distribution (SED) described by $T_d = 47$ K and $\beta = 1.6$ (see Section 4.1). Also shown is the distribution of mm flux densities of quasars from the literature (Table 3). Hashed bins indicate that the quasar host was not detected and the 3σ limit is given. Bolometer upper limits (with a typical rms of >0.5 mJy) are not shown.

1 mm flux density of the CFHQS quasars is lower than the average of our sample, the uncertainties are high. In Section 4.4 we will discuss possible correlations between the (UV) luminosity of the quasars and the brightness at millimeter wavelengths.

4. Discussion

4.1. The FIR Luminosity of $z > 6$ Quasar Host Galaxies

The shape of the FIR continuum of high-redshift quasars is often assumed to follow a modified blackbody (e.g., Priddey & McMahon 2001; Beelen et al. 2006; Leipski et al. 2014):

$$S_\nu \propto (1 - e^{-\tau_{\rm dust}}) \frac{3h\nu^3/c^2}{e^{h\nu/(kT_{\rm dust})} - 1}, \quad (1)$$

with ν being the rest-frame frequency, $\tau_{\rm dust} = (\nu/\nu_0)^\beta$ being the dust optical depth, β being the dust emissivity power-law spectral index, and $T_{\rm dust}$ being the dust temperature. The FIR luminosity, $L_{\rm FIR}$, is calculated by integrating Equation (1) between 42.5 and 122.5 μm in the rest-frame (e.g., Helou et al. 1988).

To compute the FIR luminosity we need to make assumptions on the dust temperature, spectral index, and dust optical depth. As described in Section 2.2 the ALMA observations provide measurements of the dust continuum at two different rest-frame frequencies, at roughly 1790 and 1900 GHz. The ratio of these two measurements could constrain the dust spectral energy distribution (see, for example, the discussion in Venemans et al. 2016). In Figure 4 we plot the ratio of the 1790 and 1900 GHz flux densities as a function of S/N. As expected for the dust temperatures considered here ($T_{\rm dust} > 30$ K, see below), the

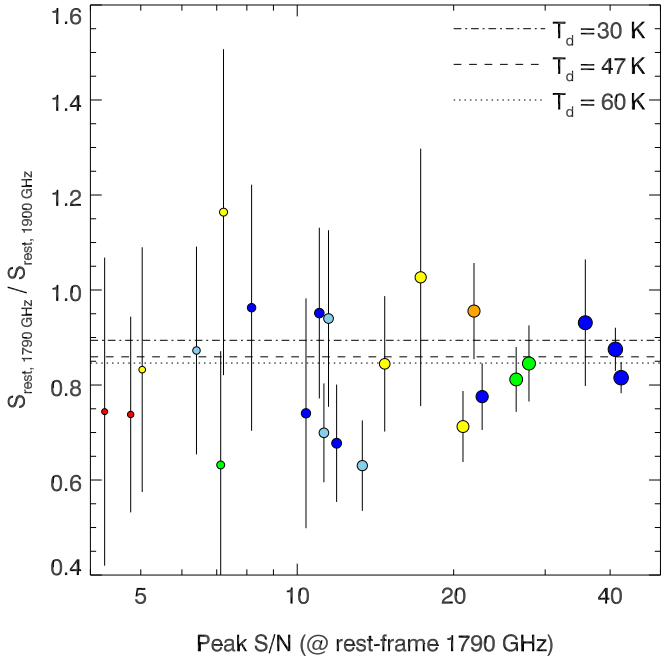

Figure 4. Ratio of the flux density at a rest-frame frequency of ∼1790 GHz to that at a rest-frame frequency of 1900 GHz as a function of S/N. The size of the symbol scales with the S/N and the colors represent the size of the emission as plotted in Figure 2. The dotted–dashed, dashed, and dotted lines indicate the ratio for a modified blackbody at $z = 6.1$ (the median redshift of our sample) with an emissivity index of $\beta = 1.6$ and a dust temperature of $T_{\rm dust} = 30$, 47, and 60 K, respectively. Within 2σ, the measurements are consistent with the fiducial dust properties ($T_{\rm dust} = 47$ K and $\beta = 1.6$).

continuum at 1900 GHz in the rest-frame is brighter than that at 1790 GHz. Within 2σ, the $S_{\rm rest,1790\,GHz}/S_{\rm rest,1900\,GHz}$ of our quasar hosts detected with an S/N > 3 at 1790 GHz is ∼0.86, the expected ratio for a fiducial modified blackbody with $T_{\rm dust} = 47$ K and $\beta = 1.6$ (the best-fit values by Beelen et al. 2006; see below). However, given that we are probing the continuum on the Rayleigh–Jeans tail of the dust emission, from our data alone we cannot derive a dust temperature together with the emissivity index, as they are degenerate. To accurately constrain the characteristics of the dust emission, we require continuum measurements at different frequencies.

Following Beelen et al. (2006) and Venemans et al. (2016), here we assume that the dust optical depth is negligible at far-infrared frequencies, i.e., $\tau_{\rm dust} \ll 1$ at rest-frame frequencies $\nu_{\rm rest} < 7.5$ THz. It should be noted that an analysis of the dust SED of high-redshift submillimeter galaxies found that the dust optical depth can be significant at rest-frame frequencies $\nu_{\rm rest} < 2$ THz (e.g., Riechers et al. 2013, 2014; Spilker et al. 2016). This would modify the derived parameters for our quasar hosts. For example, if the dust optical depth is $\tau_{\rm dust} = 1$ at $\nu_{\rm rest} = 1790$ GHz, then for a modified blackbody with $T_{\rm dust} = 35$–55 K and $\beta = 1.6$ (see below) the derived FIR luminosities will be lower by a factor of 2–3.

In the literature, several groups have measured the (average) dust temperature and emissivity index of quasar hosts. Priddey & McMahon (2001) found a dust temperature of $T_{\rm dust} = 41$ K and an emissivity index of $\beta = 1.95$ for a sample of $z \approx 4$ quasars, while Beelen et al. (2006) measured $T_{\rm dust} = 47$ K and $\beta = 1.6$. More recently, Stacey et al. (2018) parameterized the dust spectral energy distribution of a sample of gravitationally lensed quasars at $z = 1$–4 with $T_{\rm dust} = 38$ K and $\beta = 2.0$.

Alternatively, we can fit templates of the local star-forming galaxies Arp 220 and M82 (from e.g., Silva et al. 1998), bypassing the various uncertainties introduced when using Equation (1). To give an example, fitting the dust spectral energy distribution of Arp 220 with Equation (1) results in a high dust temperature of $T_{\rm dust} = 66$ K and a significant dust optical depth of $\tau_{\rm dust} \approx 2$ at a rest-frame frequency of 1900 GHz (e.g., Rangwala et al. 2011).

Following the literature on $z \sim 6$ quasars (e.g., Wang et al. 2008, 2013; Willott et al. 2013; Venemans et al. 2016), we here assume that the dust spectral energy distribution can be described by a modified blackbody with a dust temperature of $T_{\rm dust} = 47$ K and an emissivity index of $\beta = 1.6$ (e.g., Beelen et al. 2006; Leipski et al. 2014). In Table 2 we list the derived properties of the quasar hosts in our sample. As discussed above, the listed values in the table highly depend on the assumptions on the dust temperature and emissivity made here. For example, if we instead assume the best-fit values from Priddey & McMahon (2001), the FIR luminosity is lower by 11%. Using $T_{\rm dust} = 38$ K and $\beta = 2.0$ results in an FIR luminosity that is 23% lower, while with a higher dust temperature of $T_{\rm dust} = 55$ K (with $\beta = 1.6$), as found for a quasar host galaxy at $z = 6.4$ (e.g., Beelen et al. 2006), the $L_{\rm FIR}$ is 50% higher. Scaling the M82 and Arp 220 templates to our measured flux density results in an FIR luminosity that is 38% and 48% lower, respectively.

The quasars in our ALMA sample have FIR luminosities between $L_{\rm FIR} = 2.7 \times 10^{11}\,L_\odot$ and $L_{\rm FIR} = 1.3 \times 10^{13}\,L_\odot$, with a median value of $L_{\rm FIR} = 1.8 \times 10^{12}\,L_\odot$ (Table 2). Of the 27 quasars observed, 20 (74%) have FIR luminosities above $10^{12}\,L_\odot$ (the classical definition of a ULIRG). The remaining 7 (26%) have $10^{11} < L_{\rm FIR} < 10^{12}\,L_\odot$. If we include sources from the literature that fulfill our sample selection criteria (Section 2.1) and have a detection at 1 mm (Table 3), then we derive a similar median FIR luminosity of $L_{\rm FIR} = 2.1 \times 10^{12}\,L_\odot$ and a ULIRG fraction of 81%.

We stress again that the FIR luminosities derived above strongly depend on the assumed shape of the dust spectral energy distribution. Additional photometry at other FIR frequencies is needed to better constrain the FIR luminosity for our quasar host galaxies.

4.2. SFRs

For high-redshift quasars, the dominant heating source of the dust that produces the infrared radiation appears to be stars (e.g., Leipski et al. 2014; Barnett et al. 2015; Venemans et al. 2017c, but see, e.g., Schneider et al. 2015). To estimate the SFR in the $z \gtrsim 6$ quasar hosts, we can therefore apply the scaling relation found in the local universe between the total infrared (TIR) luminosity, $L_{\rm TIR}$, and the SFR: $\mathrm{SFR} = 1.48 \times 10^{-10} L_{\rm TIR}/L_\odot$ (Murphy et al. 2011). The total infrared luminosity can be obtained by integrating the dust spectral energy distribution between the rest-frame wavelengths of 3 and 1100 μm (Kennicutt & Evans 2012).

Computing TIR luminosities for our quasar hosts assuming a dust spectral energy distribution parameterized by $T_{\rm dust} = 47$ K and $\beta = 1.6$ (see Section 4.1), we derive SFRs of $\mathrm{SFR} = 50$–$2700\ M_\odot\ \mathrm{yr}^{-1}$ (Table 2). This assumes all the dust emission is heated by star formation, so these values can be considered upper limits on the obscured SFRs in the quasar host galaxies. We caution that the derived SFRs strongly depend on our assumed dust properties and the uncertainties on

the SFRs reported in Table 2 are up to a factor of ∼2–3 (see the discussion in Section 4.1). As an example, if we assume a dust temperature of $T_{\rm dust} = 55$ K (instead of $T_{\rm dust} = 47$ K) the resulting range of SFR in our quasar host galaxies is SFR = 90–4550 $M_\odot$ yr^{-1}, while fitting an Arp 220 template to our measured flux densities (see Section 4.1) lead to lower derived SFRs of SFR = 30–1650 $M_\odot$ yr^{-1}. For a comparison between the SFRs in the host galaxies derived from the dust emission and from the [C II] emission line, we refer to the discussion in Decarli et al. (2018, see their Figure 9). We caution that the derived SFRs strongly depend on our assumed dust properties and the uncertainties on the SFRs reported in Table 2 are up to a factor of ∼3 (see the discussion in Section 4.1).

Using the (highly uncertain) size estimates reported in Table 2, we estimate SFR surface densities (SFRD) ranging from SFRD = 8–376 $M_\odot$ yr^{-1} kpc^{-2}. Given the low spatial resolution of our data, the measured sizes should be considered upper limits and the SFRD could be significantly higher. Higher spatial resolution observations will provide more accurate source sizes and better constrain the SFRD (see, e.g., Walter et al. 2009).

4.3. Dust Masses in Quasar Host at $z > 6$

From the measured FIR flux density and assuming a dust temperature and emissivity index, we can estimate the total mass in dust, $M_{\rm dust}$, using the equation:

$$M_{\rm dust} = \frac{S_\nu D_L^2}{(1+z)\kappa_\nu(\beta) B_\nu(\nu, T_{\rm dust})}, \quad (2)$$

where D_L is the luminosity distance, $\kappa_\nu(\beta)$ is the dust mass opacity coefficient, and B_ν is the Planck function. The opacity coefficient is given by $\kappa_\nu(\beta) = 0.77(\nu/352\,{\rm GHz})^\beta\,{\rm cm^2\,g^{-1}}$ (e.g., Dunne et al. 2000).

Assuming $T_{\rm dust} = 47$ K, $\beta = 1.6$ and a negligible dust optical depth at $\nu_{\rm rest} = 1790$ GHz (the canonical values used in the literature for $z \sim 6$ quasar host; see Section 4.1), the estimated dust masses range from $M_{\rm dust} \approx 2 \times 10^7\,M_\odot$ for the faintest sources to nearly $M_{\rm dust} \approx 10^9\,M_\odot$ for the brightest quasar host galaxy (Table 2).

Similar to the derived FIR luminosity, these estimates of the dust mass in the quasar host galaxies are highly uncertain due to the unknown characteristics of the dust (see the discussion in Section 4.1). If the dust is parameterized by $T_{\rm dust} = 41$ K, $\beta = 1.9$ ($T_{\rm dust} = 38$ K, $\beta = 2.0$), instead of $T_{\rm dust} = 47$ K and $\beta = 1.6$ as used above, then the derived dust masses in Table 2 are ∼14% (∼11%) lower. On the other hand, scaling our measured flux densities to the templates of Arp 220 and M82 from Silva et al. (1998) results in derived dust masses that are 1.3–4.6× higher.

4.4. Correlation between the FIR and UV Luminosity

In Venemans et al. (2016) we collected all [C II] and underlying dust continuum observations of $z \gtrsim 6$ quasars from the literature and found that both the [C II] emission and the FIR luminosity positively correlate with the luminosity of the AGN. However, the quasars used to derive that correlation were selected in different ways. With our homogenous, luminosity-limited quasar sample we can revisit this topic. In Figure 5 (left) we compare the FIR luminosity of our quasars (Table 2) and all quasars from the literature (see Table 3) with the brightness of the UV continuum emitted by the accreting black hole, M_{1450} (or, equivalently, the quasar bolometric luminosity $L_{\rm bol}$, which is derived using Equation (1) in Venemans et al. 2016). Within the relatively narrow quasar luminosity range of our sample, the FIR and UV luminosities correlate only weakly, with a Pearson's r of $r = -0.37$ (a strong correlation is defined by us as $|r| > 0.5$; see, e.g., Venemans et al. 2016). Quasars with the same UV luminosity can have FIR luminosities that differ by more than one order of magnitude. Similarly, at a given FIR luminosity, the range of M_{1450} of the quasars is >3 mag. Clearly, in the early universe there are quasars with rapid black hole growth but only little (obscured) stellar mass growth. At the same time, starburst galaxies with SFRs exceeding 1000 $M_\odot$ yr^{-1} exist at $z > 6$ that do not appear to have a highly accreting massive black hole (e.g., Riechers et al. 2013; Marrone et al. 2018). Fitting a straight line to the data results in a correlation with a non-zero slope: $\log(L_{\rm FIR}) = (12.41 \pm 0.05) - (0.18 \pm 0.04) \times (M_{\rm UV}+26)$. There is a large dispersion around this fit, with a standard deviation of 0.45 dex.

Nonetheless, it is possible that this correlation is biased. For example, follow-up observations of the most UV luminous quasars were performed on the sources with bolometer detections. We therefore only plot the sources belonging to our luminosity-limited quasar sample ($M_{1450} < -25.25$, $z > 5.94$ and decl. <15°, see Section 2.1) in Figure 5 (right). In this complete sample, the correlation is even weaker, with a Pearson's $r = -0.22$. Similarly, in Decarli et al. (2018), we only find a weak correlation between M_{1450} and the [C II] luminosity, while the [C II]-to-FIR luminosity ratio is independent of the quasar brightness. This argues against a strong contribution of the AGN to the heating of the dust, consistent with earlier conclusions based on different arguments (e.g., Leipski et al. 2014; Decarli et al. 2018).

These results are consistent with studies of quasars at lower redshifts. For example, Harris et al. (2016) investigated the SFR in luminous quasars at $2 < z < 3$ and found that beyond a bolometric luminosity of $L_{\rm bol} \gtrsim 10^{13}\,L_\odot$ (corresponding roughly to $M_{1450} \sim -25.5$) the SFR is independent of the brightness of the quasar (dashed line in Figure 5). Similarly, Pitchford et al. (2016) found that the typical SFR remains constant for optically luminous quasars and does not vary with black hole mass or accretion rate.

5. Summary

In this paper we present ALMA snapshot observations (8 minutes on-source) of 27 quasars at $z \gtrsim 6$ selected from a UV luminosity-limited quasar sample. All quasars were detected in the dust continuum at an observed wavelength of ∼1 mm, although the faintest quasars have only marginal detections (S/N ≈ 3). Below, we summarize our findings. The very high detection rate of our quasars (100% in the continuum and 85% in [C II]; Decarli et al. 2018) in very short, 8 minute, integration times will allow more detailed studies (e.g., multi-band SED, high spatial resolution observations) of these quasar host galaxies in the future.

1. The quasar host galaxies in our survey span a wide range in observed millimeter continuum flux densities. The faintest quasar hosts have $S_{\rm obs,1\,mm} = 0.12$ mJy, which is among the faintest $z \sim 6$ quasar hosts observed. The brightest quasar host in our survey, with $S_{\rm obs,1\,mm} = 5.9$ mJy, is the second most luminous quasar host after J2310+1855 at $z = 6.0$

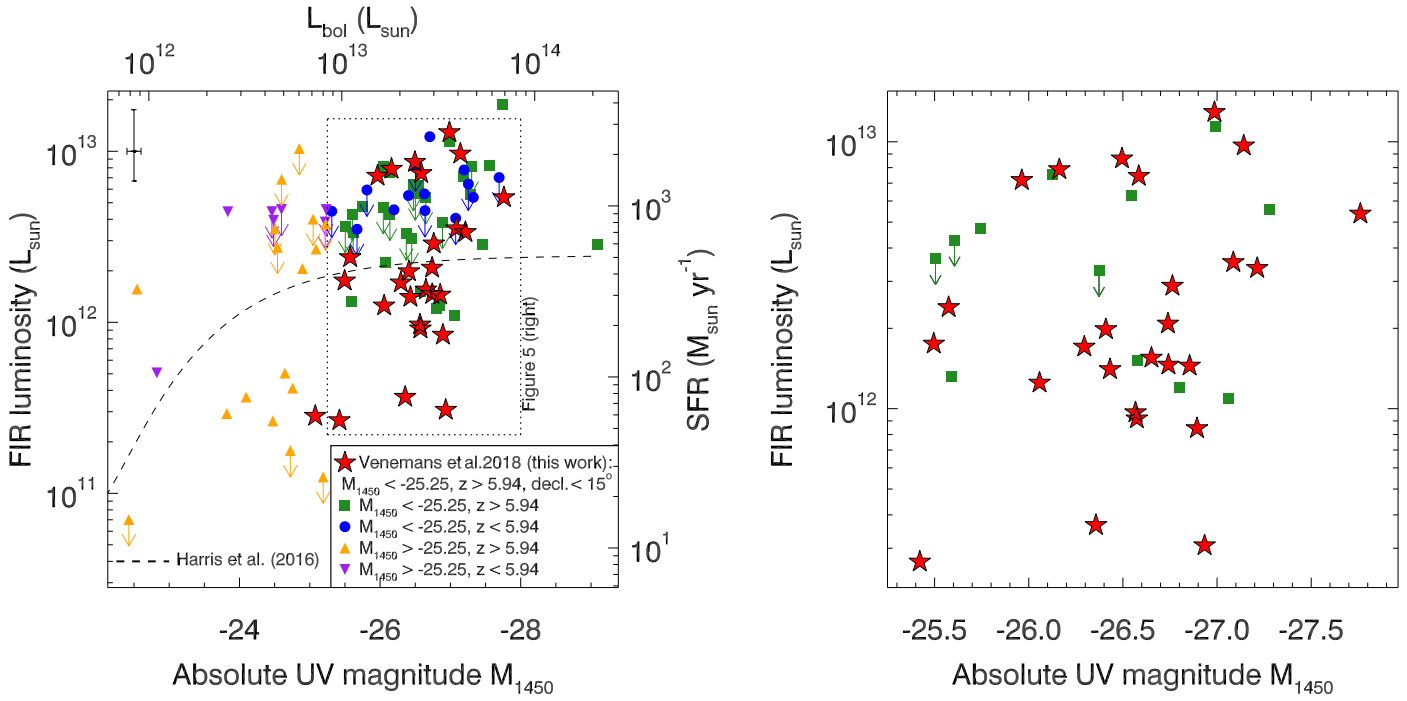

Figure 5. Left: FIR luminosity (computed assuming $T_{\rm dust} = 47$ K and $\beta = 1.6$) of $z > 5.7$ quasars as a function of the absolute magnitude $M_{\rm UV}$ at a wavelength 1450 Å in the rest-frame. Undetected objects are plotted with 3σ upper limits (downward arrows). In the upper left corner the typical error bar is plotted. The dashed line is the relation between SFR and $L_{\rm bol}$ for quasars at $2 < z < 3$ (Harris et al. 2016). A zoomed-in view of the dotted region is shown on the right. Right: same as the left plot, but this time for our quasar luminosity-limited ($M_{1450} < -25.25$) sample of $z \gtrsim 6$ quasars. Within the small UV luminosity range probed by our survey, no correlation is evident between the brightness of the quasar and the luminosity of the dust emission in the host galaxy, with a large scatter in FIR luminosity for a given quasar brightness.

(Wang et al. 2013). The median flux density of quasar host galaxies in our survey is $S_{\rm obs,1\ mm} = 0.9$ mJy, very similar to the first bolometer results.

2. As a result of the low spatial resolution of our observations (beam sizes around 1″, or ∼5.7 kpc), 63% of the quasar hosts detected at S/N > 10 remain unresolved. The remaining quasar host are marginally resolved and have deconvolved sizes of 3.3–6.9 kpc.
3. The FIR luminosities, implied by the continuum measurements, are between $L_{\rm FIR} = 3 \times 10^{11}\,L_\odot$ and $L_{\rm FIR} = 1 \times 10^{13}\,L_\odot$, assuming a dust temperature of 47 K and an emissivity index of $\beta = 1.6$. A high fraction of 70% of quasars in our survey are hosted by ULIRGs. For a complete sample of quasars with $M_{1450} < -25.25$, the fraction of ULIRGs is 78%.
4. If the dust is heated by star formation, the SFR implied by the infrared emission is 50–2700 $M_\odot$ yr^{-1}. The derived dust masses in the quasar host galaxies are $M_{\rm dust} = 2 \times 10^7 - 1 \times 10^9\,M_\odot$, implying significant amounts of dust and metals have been produced in these galaxies within 1 Gyr after the Big Bang.
5. Although the quasar hosts are marginally resolved at best, we can use the (upper limits on) the sizes to estimate star formation rate densities (SFRDs). From the derived SFRs, we calculate SFRD = 10–400 $M_\odot$ yr^{-1} kpc^{-2}. These should be considered lower limits as the size of the continuum emission could be significantly smaller than the limits presented in Table 2; see, e.g., Wang et al. (2013), Venemans et al. (2016).

In the local universe, a relation between the mass of a black hole and the bulge mass of the galaxy host has been reported (e.g., Kormendy & Ho 2013). This has frequently been discussed in the context of a coevolution between the central black hole and the galaxy, i.e., that accretion onto the central black hole (black hole growth) should be accompanied by star formation (stellar growth), but see Jahnke & Macciò (2011) for a different interpretation of this observational finding.

The apparent lack of a correlation between black hole accretion (as measured by the UV luminosity) and stellar mass growth (as measured through the FIR luminosity) reported in this study could therefore indicate that black holes and the host galaxy do in fact not co-evolve, at least in the case of the most luminous quasars in the first Gyr of the universe.

This was also concluded by a different set of arguments by other studies of $z > 6$ quasars, i.e., some dynamical mass estimates of quasar host galaxies indicate that they are under–massive compared to the supermassive black holes that they host (e.g., Walter et al. 2004; Venemans et al. 2016; Decarli et al. 2018; but see, e.g., Willott et al. 2015 for lower–luminosity counterexamples).

There are several other interpretations of the apparent lack of correlation between black hole accretion and star formation. For example, extinction of the UV quasar emission along the line of sight could introduce a significant amount of scatter. Similarly, if quasar host galaxies have a range of dust temperatures, our assumption that all hosts have $T_{\rm dust} = 47$ K will result in additional scatter. Alternatively, a more physical interpretation is that the timescales of black hole accretion could be much smaller than those of star formation. The measured radiation due to accretion onto a black hole can in principle vary over a timescale of years (given the small size of the emitting broad line region; see, e.g., Krumpe et al. 2017), whereas the star formation rate tracer used here, the FIR emission, has much longer timescales, $\gtrsim 10^8$ year

(e.g., Hickox et al. 2012). In this scenario, the weak correlation between SFR and quasar luminosity is probably mainly caused by the variability of the central source (see, e.g., Hickox et al. 2014). Finally, the absence of a clear correlation could also be explained by an evolutionary scenario that links infrared luminous starburst galaxies and bright quasars (e.g., Sanders et al. 1988; Alexander & Hickox 2012). In this scenario, the black hole grows rapidly in a dusty galaxy with a high SFR. The feedback of the luminous AGN removes the dusty interstellar medium, resulting in a UV-bright quasar. Simultaneously, the strong feedback removes the fuel for star formation, and therefore suppresses the FIR luminosity (e.g., Lapi et al. 2014; Mancuso et al. 2016). With the available data it is difficult to differentiate between these different interpretations.

One way forward is to increase the UV luminosity range of the sample and investigate the host galaxy properties of fainter quasars. Studies of a small number of such low-luminosity quasars already suggest that the FIR luminosity of these quasars is on average lower (e.g., Willott et al. 2013, 2017; Izumi et al. 2018), although, at the same time, there are galaxies with $L_{\rm FIR} > 10^{13}\,L_{\odot}$ that do not show any black hole accretion (e.g., Riechers et al. 2013; Marrone et al. 2018). A better method to determine if the black hole and stellar mass of distant quasars grow simultaneously is to directly compare the mass of the black hole with the mass of stars in the host galaxy. In the near future, observations with the *James Webb Space Telescope* opens up the potential to detect the stars in the host galaxies. From the derived stellar masses it will be more straightforward to identify whether the first supermassive black holes already follow the local scaling relations.

We thank the referee for providing valuable comments and suggestions. B.P.V., F.W., and E.P.F. acknowledge funding through the ERC grants "Cosmic Dawn" and "Cosmic Gas." Part of the support for R.D. was provided by the DFG priority program 1573 "The physics of the interstellar medium." D.R. acknowledges support from the National Science Foundation under grant number AST-1614213. This paper makes use of the following ALMA data: ADS/JAO.ALMA#2015.1.01115.S. ALMA is a partnership of ESO (representing its member states), NSF (USA) and NINS (Japan), together with NRC (Canada) and NSC and ASIAA (Taiwan), in cooperation with the Republic of Chile. The Joint ALMA Observatory is operated by ESO, AUI/NRAO, and NAOJ.

Facility: ALMA.

ORCID iDs

Bram P. Venemans https://orcid.org/0000-0001-9024-8322
Roberto Decarli https://orcid.org/0000-0002-2662-8803
Fabian Walter https://orcid.org/0000-0003-4793-7880
Eduardo Bañados https://orcid.org/0000-0002-2931-7824
Frank Bertoldi https://orcid.org/0000-0002-1707-1775
Xiaohui Fan https://orcid.org/0000-0003-3310-0131
Emanuele Paolo Farina https://orcid.org/0000-0002-6822-2254
Chiara Mazzucchelli https://orcid.org/0000-0002-5941-5214
Dominik Riechers https://orcid.org/0000-0001-9585-1462
Hans-Walter Rix https://orcid.org/0000-0003-4996-9069
Yujin Yang https://orcid.org/0000-0003-3078-2763

References

Alexander, D. M., & Hickox, R. C. 2012, NewAR, 56, 93
Bañados, E., Decarli, R., Walter, F., et al. 2015, ApJL, 805, L8
Bañados, E., Venemans, B. P., Decarli, R., et al. 2016, ApJS, 227, 11
Bañados, E., Venemans, B. P., Mazzucchelli, C., et al. 2018, Natur, 553, 473
Barnett, R., Warren, S. J., Banerji, M., et al. 2015, A&A, 575, A31
Beelen, A., Cox, P., Benford, D. J., et al. 2006, ApJ, 642, 694
Bertoldi, F., Carilli, C. L., Cox, P., et al. 2003a, A&A, 406, L55
Bertoldi, F., Cox, P., Neri, R., et al. 2003b, A&A, 409, L47
Carilli, C. L., Wang, R., Fan, X., et al. 2010, ApJ, 714, 834
Champagne, J. B., Decarli, R., Casey, C. M., et al. 2018, arXiv:1809:10178
Cool, R. J., Kochanek, C. S., Eisenstein, D. J., et al. 2006, AJ, 132, 823
De Rosa, G., Decarli, R., Walter, F., et al. 2011, ApJ, 739, 56
Decarli, R., Walter, F., Venemans, B. P., et al. 2017, Natur, 545, 457
Decarli, R., Walter, F., Venemans, B. P., et al. 2018, ApJ, 854, 97
Decarli, R., Walter, F., Yang, Y., et al. 2012, ApJ, 756, 150
Dunne, L., Eales, S., Edmunds, M., et al. 2000, MNRAS, 315, 115
Fan, X., Strauss, M. A., Becker, R. H., et al. 2006, AJ, 132, 117
Gallerani, S., Ferrara, A., Neri, R., & Maiolino, R. 2014, MNRAS, 445, 2848
Harris, K., Farrah, D., Schulz, B., et al. 2016, MNRAS, 457, 4179
Helou, G., Khan, I. R., Malek, L., & Boehmer, L. 1988, ApJS, 68, 151
Hickox, R. C., Mullaney, J. R., Alexander, D. M., et al. 2014, ApJ, 782, 9
Hickox, R. C., Wardlow, J. L., Smail, I., et al. 2012, MNRAS, 421, 284
Hopkins, P. F., Hernquist, L., Cox, T. J., & Kereš, D. 2008, ApJS, 175, 356
Izumi, T., Onoue, M., Shirakata, H., et al. 2018, PASJ, 70, 36
Jahnke, K., & Macciò, A. V. 2011, ApJ, 734, 92
Jiang, L., Fan, X., Annis, J., et al. 2008, AJ, 135, 1057
Jiang, L., Fan, X., Bian, F., et al. 2009, AJ, 138, 305
Jiang, L., McGreer, I. D., Fan, X., et al. 2016, ApJ, 833, 222
Kennicutt, R. C., & Evans, N. J. 2012, ARA&A, 50, 531
Kormendy, J., & Ho, L. C. 2013, ARA&A, 51, 511
Kroupa, P., & Weidner, C. 2003, ApJ, 598, 1076
Krumpe, M., Husemann, B., Tremblay, G. R., et al. 2017, A&A, 607, L9
Kurk, J. D., Walter, F., Fan, X., et al. 2007, ApJ, 669, 32
Kurk, J. D., Walter, F., Fan, X., et al. 2009, ApJ, 702, 833
Lapi, A., Raimundo, S., Aversa, R., et al. 2014, ApJ, 782, 69
Leipski, C., Meisenheimer, K., Walter, F., et al. 2014, ApJ, 785, 154
Maiolino, R., Cox, P., Caselli, P., et al. 2005, A&A, 440, L51
Mancuso, C., Lapi, A., Shi, J., et al. 2016, ApJ, 833, 152
Marrone, D. P., Spilker, J. S., Hayward, C. C., et al. 2018, Natur, 553, 51
Matsuoka, Y., Onoue, M., Kashikawa, N., et al. 2018, PASJ, 70, S35
Mazzucchelli, C., Bañados, E., Venemans, B. P., et al. 2017, ApJ, 849, 91
McGreer, I. D., Becker, R. H., Helfand, D. J., & White, R. L. 2006, ApJ, 652, 157
Mechtley, M., Windhorst, R. A., Ryan, R. E., et al. 2012, ApJL, 756, L38
Mortlock, D. J., Patel, M., Warren, S. J., et al. 2009, A&A, 505, 97
Murphy, E. J., Condon, J. J., Schinnerer, E., et al. 2011, ApJ, 737, 67
Omont, A., Willott, C. J., Beelen, A., et al. 2013, A&A, 552, A43
Petric, A. O., Carilli, C. L., Bertoldi, F., et al. 2003, AJ, 126, 15
Pitchford, L. K., Hatziminaoglou, E., Feltre, A., et al. 2016, MNRAS, 462, 4067
Planck Collaboration, Ade, P. A. R., Aghanim, N., et al. 2016, A&A, 594, A13
Priddey, R. S., & McMahon, R. G. 2001, MNRAS, 324, L17
Rangwala, N., Maloney, P. R., Glenn, J., et al. 2011, ApJ, 743, 94
Reines, A. E., & Volonteri, M. 2015, ApJ, 813, 82
Riechers, D. A., Bradford, C. M., Clements, D. L., et al. 2013, Natur, 496, 329
Riechers, D. A., Carilli, C. L., Capak, P. L., et al. 2014, ApJ, 796, 84
Riechers, D. A., Walter, F., Bertoldi, F., et al. 2009, ApJ, 703, 1338
Sanders, D. B., Soifer, B. T., Elias, J. H., et al. 1988, ApJ, 325, 74
Schneider, R., Bianchi, S., Valiante, R., Risaliti, G., & Salvadori, S. 2015, A&A, 579, A60
Shao, Y., Wang, R., Jones, G. C., et al. 2017, ApJ, 845, 138
Silva, L., Granato, G. L., Bressan, A., & Danese, L. 1998, ApJ, 509, 103
Spilker, J. S., Marrone, D. P., Aravena, M., et al. 2016, ApJ, 826, 112
Stacey, H. R., McKean, J. P., Robertson, N. C., et al. 2018, MNRAS, 476, 5075
Tadaki, K.-i., Genzel, R., Kodama, T., et al. 2017, ApJ, 834, 135
Venemans, B. P., McMahon, R. G., Walter, F., et al. 2012, ApJL, 751, L25
Venemans, B. P., Walter, F., Decarli, R., et al. 2017a, ApJ, 837, 146
Venemans, B. P., Walter, F., Decarli, R., et al. 2017b, ApJL, 851, L8
Venemans, B. P., Walter, F., Decarli, R., et al. 2017c, ApJ, 845, 154
Venemans, B. P., Walter, F., Zschaechner, L., et al. 2016, ApJ, 816, 37
Walter, F., Bertoldi, F., Carilli, C., et al. 2003, Natur, 424, 406
Walter, F., Carilli, C., Bertoldi, F., et al. 2004, ApJ, 615, L17
Walter, F., Riechers, D., Cox, P., et al. 2009, Natur, 457, 699
Wang, F., Fan, X., Yang, J., et al. 2017, ApJ, 839, 27

Wang, R., Carilli, C. L., Beelen, A., et al. 2007, AJ, 134, 617
Wang, R., Carilli, C. L., Neri, R., et al. 2010, ApJ, 714, 699
Wang, R., Carilli, C. L., Wagg, J., et al. 2008, ApJ, 687, 848
Wang, R., Wagg, J., Carilli, C. L., et al. 2011a, ApJL, 739, L34
Wang, R., Wagg, J., Carilli, C. L., et al. 2011b, AJ, 142, 101
Wang, R., Wagg, J., Carilli, C. L., et al. 2013, ApJ, 773, 44
Wang, R., Wu, X.-B., Neri, R., et al. 2016, ApJ, 830, 53
Willott, C. J., Albert, L., Arzoumanian, D., et al. 2010a, AJ, 140, 546
Willott, C. J., Bergeron, J., & Omont, A. 2015, ApJ, 801, 123
Willott, C. J., Bergeron, J., & Omont, A. 2017, ApJ, 850, 108
Willott, C. J., Delorme, P., Omont, A., et al. 2007, AJ, 134, 2435
Willott, C. J., Delorme, P., Reylé, C., et al. 2009, AJ, 137, 3541
Willott, C. J., Delorme, P., Reylé, C., et al. 2010b, AJ, 139, 906
Willott, C. J., Omont, A., & Bergeron, J. 2013, ApJ, 770, 13